Title

Performance-limiting formation dynamics in mixed-halide perovskites

Authors

Huang, Tianyi
Tan, Shaun
Nuryyeva, Selbi
et al.

MATERIALS SCIENCE

Performance-limiting formation dynamics in mixed-halide perovskites

Tianyi Huang[1,2]†, Shaun Tan[1,2]†, Selbi Nuryyeva[3]†, Ilhan Yavuz[4]*, Finn Babbe[2],
Yepin Zhao[1], Maged Abdelsamie[5], Marc H. Weber[6], Rui Wang[1], Kendall N. Houk[3],
Carolin M. Sutter-Fella[2,7]*, Yang Yang[1]*

Wide-bandgap (WBG) mixed-halide perovskites as the front cell absorber are accomplishing perovskite-based tandem solar cells with over 29% power conversion efficiency. However, their large voltage deficits limit their ultimate performance. Only a handful of studies probe the fundamental mechanisms underlying the voltage deficits, which remain an unsolved challenge in the field. In this study, we investigate the formation dynamics and defect physics of WBG mixed-halide perovskites in contrast with their corresponding triiodide-based perovskites. Our results show that the inclusion of bromide introduced a halide homogenization process that occurs during the perovskite growth stage from an initial bromide-rich phase toward the final target stoichiometry. We further elucidated a physical model that correlates the role of bromide with the formation dynamics, defect physics, and eventual optoelectronic properties of the film. This work provides a fundamental and unique perspective toward understanding the performance-limiting factors affecting WBG mixed-halide perovskites.

INTRODUCTION

Metal halide perovskites with their X-sites of iodine partially substituted with bromine have demonstrated great potential for commercialization of halide perovskite technology for use in tandem photovoltaics (PVs) integrated with conventional PV products such as Si and CuInGaSe$_2$ (CIGS) (1). By controlling the I/Br ratio, the optical bandgaps of mixed-halide perovskites can be tuned to be between 1.64 and 1.70 eV, usually referred to as wide-bandgap (WBG) perovskites in the field, ideal for front-cell applications in two-junction tandem PVs (2). With such WBG mixed-halide perovskites, perovskite-Si and perovskite-CIGS tandem cells have reached remarkable power conversion efficiencies (PCEs) of 29.5 and 24.2%, respectively (3).

Conversely, single-junction PVs based on most FAPbI$_3$ triiodide perovskite compositions (E_g = 1.48 eV, $V_{OC, SQ}$ = 1.21 V, and $V_{OC, reported}$ = 1.18 V) have recently exceeded 25% PCE, with voltage deficits, defined as the difference between the optical bandgap and open-circuit voltage (V_{OC}), as low as 0.30 V (4). For WBG mixed-halide perovskites, however, currently, even the best reported subcell with hole transporting materials with negligible energy offsets with the perovskite layer exhibited a voltage deficit up to 0.46 V (E_g = 1.68 eV, $V_{OC, SQ}$ = 1.40 V, and $V_{OC, reported}$ = 1.22 V) (5). Therefore, the voltage deficits in WBG perovskites continue to lag their corresponding single-junction counterparts. Active debate is ongoing regarding the mechanistic reasons underlying the large voltage deficits in

WBG perovskites, which remains an unsolved challenge in the field. Arguably, the voltage deficits remain the largest bottleneck toward further improving the performance of perovskite-based tandem PVs.

Voltage deficits are directly correlated with nonradiative energy losses. Although halide perovskites are reported to have high defect tolerance (6, 7), deep traps still do exist, especially toward the top surface region (8), that may induce trap-mediated recombination losses (9). Intrinsic defects form during the nucleation and growth stages of the perovskite crystals from solution, and their formation is highly dependent on several processing conditions and especially the precursor stoichiometry and composition. On this note, since the cation itself minimally affects the optical bandgap, cation engineering has been intensively studied and explored. For example, Qin et al. (10) reported that formulations with Cs$^+$ markedly affected the perovskite formation dynamics and processing window, which was subsequently found by Correa-Baena et al. (11) to be also essential to achieve homogeneous halide distribution and is critical for highly efficient mixed-halide perovskite PVs. These pioneering works have provided many insights into the cations' role in preparing mixed-halide perovskites and particularly their effects on achieving halide homogeneity and preventing halide segregation during operation (5, 12–14). However, given that the halide ratio in WBG compositions is mostly preserved to achieve the necessary optical bandgap, the role of the anion on the perovskite formation dynamics has been largely unexplored. The I/Br ratio may potentially alter the nucleation and growth behaviors of WBG perovskites, which may further be related to the defect physics and optoelectronic properties of the films.

In this work, we investigated the role of Br mixing on the formation dynamics of WBG perovskites. Combining systematic experimental studies with first-principle calculations, our observations suggest that the representative FAMACsPb(I$_{0.8}$Br$_{0.2}$)$_3$ perovskite (FA=Formamidinium, MA=Methylammonium, and Cs=Cesium) undergoes a complex crystallization pathway by first nucleating a Br-rich phase from solution during supersaturation before experiencing a retarded growth stage during perovskite growth. The slow growth stage is associated with a halide homogenization process

[1]Department of Materials Science and Engineering and California NanoSystems Institute, University of California Los Angeles, Los Angeles, CA 90095, USA. [2]Chemical Sciences Division, Lawrence Berkeley National Laboratory, Berkeley, CA 94720, USA. [3]Department of Chemistry, University of California, Los Angeles, CA 90095, USA. [4]Department of Physics, Marmara University, 34722 Ziverbey, Istanbul, Turkey. [5]Materials Sciences Division, Lawrence Berkeley National Laboratory, Berkeley, CA 94720, USA. [6]Center for Materials Research, Washington State University, Pullman, WA 99164, USA. [7]Molecular Foundry, Lawrence Berkeley National Laboratory, Berkeley, CA 94720, USA.
*Corresponding author. Email: yangy@ucla.edu (Y.Y.); csutterfella@lbl.gov (C.M.S.-F.); ilhan.yavuz@marmara.edu.tr (I.Y.)
†These authors contributed equally to this work.

that brings the lattice composition to the eventual target stoichiometry. This homogenization process inadvertently altered the formation dynamics of mixed-halide perovskites and promoted defect formation, which consequently led to increased nonradiative recombination losses in the final perovskite film. In other words, Br affected the perovskite formation dynamics, which may have contributed to the large voltage deficits in high Br%-containing compositions.

RESULTS

We specifically focused on the triple cation mixed-halide WBG perovskite $FAMACsPb(I_{0.8}Br_{0.2})_3$, as it is one of the most widely reported compositions with a good resistance against light-induced halide segregation and also high PV performance. The triiodide reference with the same triple cations, $FAMACsPbI_3$, will serve as the reference to investigate the effects of Br inclusion on the perovskite formation dynamics. As shown in both the digital photographs (Fig. 1A) and absorption spectra (Fig. 1B) of the two perovskites, the as-cast $FAMACsPbI_3$ film already exhibited strong band edge absorption, indicating that the α-phase perovskite has partially formed. In contrast, the as-cast $FAMACsPb(I_{0.8}Br_{0.2})_3$ film was more transparent and showed negligible absorption associated with its perovskite phase near its target bandgap of approximately 1.67 eV (745 nm). After annealing, the band edge absorptions and absorption coefficients for both compositions were similar (but displaced in wavelength), hinting that the formation dynamics during crystallization have been altered by the inclusion of Br. We further investigated the films using x-ray diffraction (XRD). Both as-cast films exhibited the α-perovskite (001) peak. Upon annealing, the (001) peak position for $FAMACsPb(I_{0.8}Br_{0.2})_3$ underwent a notably larger shift toward lower 2θ (Fig. 1C and fig. S1), whereas the peak position for $FAMACsPbI_3$ changed negligibly in comparison. Decreasing Br content in the perovskite lattice would increase the lattice constant (smaller 2θ); therefore, the XRD results perhaps suggest that a Br-rich phase nucleated initially, and the lattice Br ratio is decreasing during the growth stage due to gradual iodide incorporation into the perovskite nuclei during crystallization [the FACs (MA-free) system was also explored in detail; see figs. S2 to S3]. Furthermore, although the cation composition is fixed as a constant for the above-discussed perovskite films, we further analyzed the XRD patterns of $MAPb(I_xBr_{1-x})_3$, $FAPb(I_xBr_{1-x})_3$ (with or without MACl additive), $FAMACsPb(I_xBr_{1-x})_3$, and $FACsPb(I_xBr_{1-x})_3$ films to rule out any possible contribution by the cations and the MACl additive (figs. S5 to S9; detailed discussion in Supplementary Text), and the observations from these "single cation" and the "MACl-free" films were consistent with the triple-cation system with MACl that delivered the champion performance. Therefore, we hypothesized that the initial nucleation was most likely dominated by a Br-rich phase, which is followed by slower iodide incorporation during the growth stage. We also observed that PbI_2 formed more readily in $FAMACsPb(I_{0.8}Br_{0.2})_3$, and the film crystallinity was poorer than $FAMACsPbI_3$ (fig. S1; detailed discussion in Supplementary Text).

To investigate such a hypothesis, we used in situ photoluminescence (PL) to monitor the perovskite crystallization process in real time. In contrast to diffraction methods, in situ PL provides direct proof of the bandgap evolution during growth, which is dominated mainly by the halide ratio in halide perovskites and thus is valuable to probe the formation dynamics related to the halide elements in real time. A 532-nm laser diode, coupled with a visible range spectrometer, was mounted in an N_2 glove box to track the film photoemission during nucleation and growth. As shown in Fig. 2A, the experiment was designed to collect the PL signal during the approximately 1 min of spin-coating step, followed by annealing at 65°C for 5 min. Figure 2 (B and C) depicts the PL spectra evolution during the formation of the mixed-halide $FAMACsPb(I_{0.8}Br_{0.2})_3$ and triiodide $FAMACsPbI_3$; data displayed on the left initiates from antisolvent dripping during spin coating. Figure S10 exemplifies the Gaussian fitting of the in situ PL spectra to extract the PL peak position, intensity, and full width at half maximum (FWHM), as plotted in Fig. 2 (D to F). It was observed that, for both formulations, their respective PL signals initiated at much higher energy levels [1.88 eV for $FAMACsPb(I_{0.8}Br_{0.2})_3$ and 1.67 eV for $FAMACsPbI_3$] compared with the final bandgap of the bulk perovskite films (approximately 1.67 and 1.57 eV, respectively, from their PL maxima). For $FAMACsPb(I_{0.8}Br_{0.2})_3$, the energy shifted by 0.115 eV during the spin-coating stage (ΔE_1) and 0.051 eV upon annealing (ΔE_2). The corresponding values were 0.072 and 0.011 eV for $FAMACsPbI_3$, much less than the mixed-halide composition. We speculated that the emission peak shifting during the perovskite formation, especially during the early growth period, could be attributed to a combination of two effects: (i) The quantum confinement of the nanograins, in which case a larger initial crystal size would show smaller energy
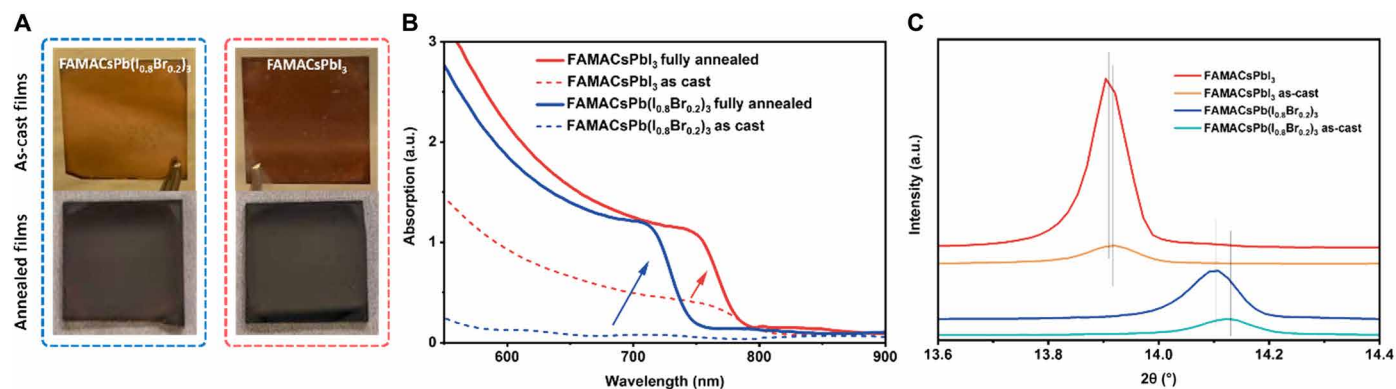

Fig. 1. Abnormal formation dynamics in WBG mixed-halide perovskites. (A) Photographs of the as-cast (top) and fully annealed (bottom) perovskite films with the stoichiometries of $CsFAMAPb(I_{0.8}Br_{0.2})_3$ (left) and $CsFAMAPbI_3$ (right). **(B)** Absorption spectra of $FAMACsPbX_3$ films before (as-cast)/after fully annealed. **(C)** XRD spectra of (001) peak of $FAMACsPbX_3$ films. a.u., arbitrary units.
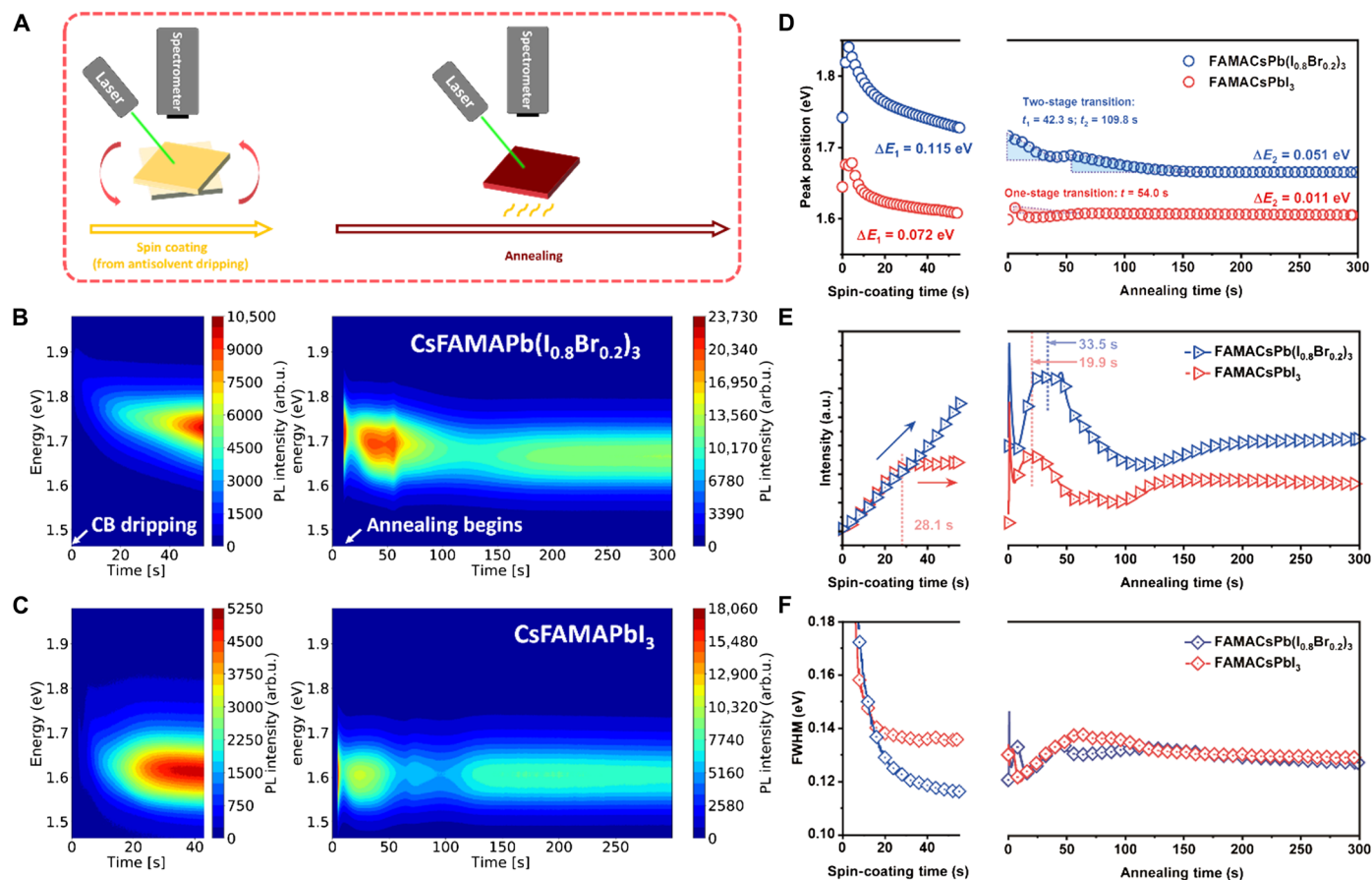
Fig. 2. In situ PL measurements monitoring the formation kinetics of perovskite films. (**A**) Illustration of the in situ PL measurement during spin-coating and annealing stage of perovskite formation. The contour plot of the captured PL spectra during the growth of (**B**) CsFAMAPb($I_{0.8}Br_{0.2})_3$ and (**C**) CsFAMAPbI$_3$ films during spin coating (left) and annealing (right). The extracted values of emission peak position (**D**), PL intensity (**E**), and FWHM (**F**) from the in situ PL measurements.

shifting; and (ii) a compositional evolution during perovskite formation dominated by an initial higher bandgap species (*15–17*). Therefore, the larger ΔE in FAMACsPb($I_{0.8}Br_{0.2})_3$ is most likely due to the formation of an initial Br-rich nuclei, complementing the XRD analysis discussed.

On the other hand, the FAMACsPbI$_3$ film took only ~54 s to reach its stable emission peak position during annealing, while for FAMACsPb($I_{0.8}Br_{0.2})_3$, the emission peak shifting lasted for over 150s. Therefore, the growth stage has been retarded in FAMACsPb($I_{0.8}Br_{0.2})_3$, likely associated with an increased activation energy barrier for perovskite growth (*18*). The emission peak transition during annealing for FAMACsPb($I_{0.8}Br_{0.2})_3$ underwent two separate stages (denoted as t_1 beginning at 42.3 s and t_2 beginning at 109.8 s) before its stabilization. We further compared the growth evolution with different amounts of Br incorporation of 20, 10, 5, and 0% (fig. S11), observing that the growth stage successively retarded further with increasing Br%. The PL intensity (Fig. 2E) observed during the growth process was a combination of several effects, including the formation of increasing amounts of highly illuminating perovskite phase crystals, countered by self-absorption as the perovskite amount increases, especially close to the band edge. As the size and specific area of crystalline perovskite change during growth, trap-assisted nonradiative recombination could also play a dominant role. Overall, we found that the PL intensity increases during the spin-coating stage, while

it continued to increase to a maximum in tens of seconds, and then decreases before the signal stabilizes during the annealing stage. We speculate that the formation of illuminating perovskite crystals dominated the PL intensity during spin coating, while during annealing, the time required to reach the intensity maximum serves as an indicator of the crystal growth rate (i.e., the earlier it reaches the intensity maximum, the faster is the growth rate). For FAMACsPbI$_3$, we observed that the signal quickly "saturated" after 28.1 s upon casting the antisolvent, while the intensity of FAMACsPb($I_{0.8}Br_{0.2})_3$ continued to increase during spin coating (Fig. 2E, left slab). During the annealing stage, these two compositions reached their maximum intensities at 33.5 and 19.9 s, respectively. Analyzing the FWHM (Fig. 2F), the signal from FAMACsPb($I_{0.8}Br_{0.2}$) achieved a much sharper peak during spin coating and stabilized slower than that of the FAMACsPbI$_3$. For the fully annealed films shown in fig. S12, both compositions exhibited clear and monopeak PL, indicating that both films eventually reached their target stoichiometry with good phase homogeneity, and matched well with their absorption cutoffs. The bandgaps were determined to be approximately 1.56 and 1.67 eV for the as prepared FAMACsPbI$_3$ and FAMACsPb($I_{0.8}Br_{0.2})_3$ films, respectively. This indicates that a halide homogenization process must have occurred during the growth stage to achieve the target stoichiometry from the initial Br-rich phase. Such a homogenization process occurs by diffusion of iodide to incorporate into the initial

Br-rich phase, which introduces an activation energy barrier and is consistent with a retardation of the perovskite growth (*19*). We further explored the FACs (MA-free) composition, which has also been reported to be highly resistant to halide segregation and delivers high PCE. The trends were consistent with the triple-cation system (figs. S13 and S14; for detailed discussion, see Supplementary Text), supporting our hypothesis and demonstrating the universal role of Br.

In addition to changing the perovskite lattice constant and bandgap, our above analyses suggest that bromide affected the perovskite formation dynamics. Bromide and iodide have different solubility with the coordinating solvents used for perovskite deposition, such as dimethylformamide (DMF), dimethyl sulfoxide (DMSO), and gamma-Butyrolactone (GBL). We further used density functional theory (DFT) to calculate the interaction energies of $PbXX'$ (X and X' denote either I or Br) species with DMSO. DMSO is partially removed by the antisolvent during spin coating, but the remaining residuals

would form an adduct phase with $PbXX'$ and FAX to assist with the formation of the α-phase perovskite (*20, 21*). From the optimized molecular configurations and bond distances shown in Fig. 3A and the interaction energies summarized in Fig. 3B, DMSO bonds most strongly with PbI_2 (0.84 eV), followed by PbIBr (0.79 eV), and has the weakest bond with $PbBr_2$ (0.77 eV), indicating that Br-rich species have lower solubility and therefore potentially nucleate first during supersaturation. Moreover, the formation energies for the $PbXX'$:DMSO adduct crystals were also calculated (fig. S16 includes the optimized crystal structures). The formation energies decreased as I was gradually replaced by Br (−0.18 eV for PbI_2:DMSO, −1.10 eV for PbIBr:DMSO, and −1.32 eV for $PbBr_2$:DMSO), suggesting that bromide-containing intermediate adduct phases are more thermodynamically favored to form. The surface energies between the triiodide perovskites with various A-site cations were also calculated to be much higher than that of the tribromide perovskites, regardless of
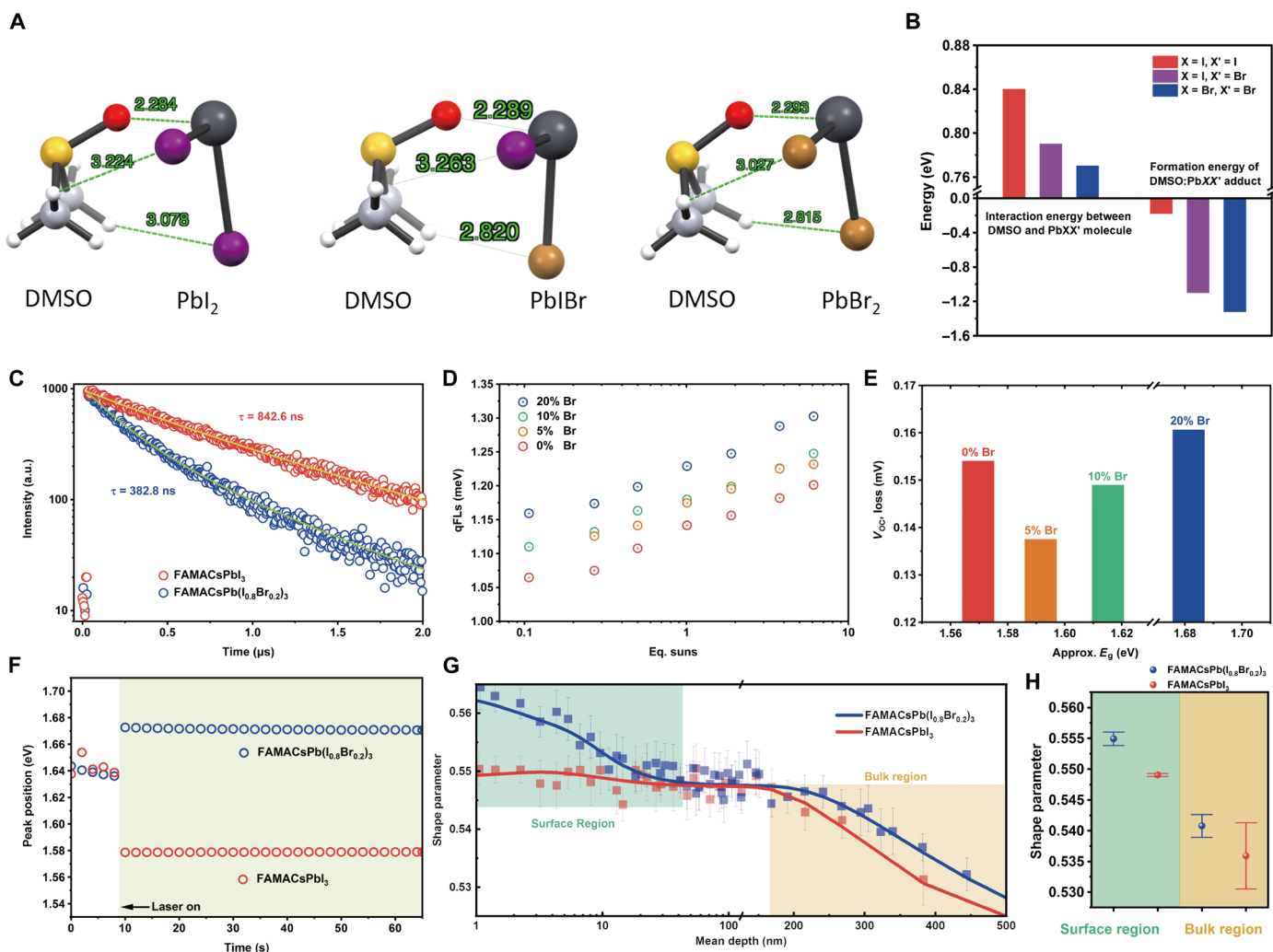

Fig. 3. First-principle calculations and characterizations of the fully annealed perovskite films. (A) Molecular configuration and interaction distance of coordinating solvent DMSO and $PbXX'$ molecules. **(B)** Interaction energy between DMSO and $PbXX'$ molecule and formation energy of DMSO:$PbXX'$ adduct phase. **(C)** Time-resolved PL spectra of the as-prepared CsFAMAPb($I_{0.8}Br_{0.2}$)$_3$ and CsFAMAPbI$_3$ films. **(D)** Quasi-Fermi level splitting (qFL) results quantified by a calibrated laser intensity and **(E)** the as-extracted $V_{OC,loss}$ ($V_{OC,SQ}$ − qFLs) for perovskite films with Br% of 20, 10, 5, and 0%. **(F)** The extracted values of emission peak position from 60-s PL tracking. **(G)** PAS depth profiling of CsFAMAPb($I_{0.8}Br_{0.2}$)$_3$ and CsFAMAPbI$_3$ films. Solid lines are fitted plots. Green/orange shaded areas indicate the top surface/bulk region of the films. **(H)** Shape parameters from PAS extracted for the surface/bulk regions.

the A-site cation (either PbX_2 or X-site termination; fig. S17), indicating that Br species preferentially nucleate first, given that surface free energy increases the total free energy of nucleation. Taking the theoretical results altogether, bromide-containing species are therefore thermodynamically more favored to form compared to iodide-containing species and therefore complement the experimental observations that bromide-rich species formed first during the initial nucleation stage.

Both the experimental and theoretical results are complementary in showing that bromide drastically altered the perovskite formation dynamics by (i) promoting the initial nucleation of a bromide-rich species and (ii) introducing an anion exchange–like halide homogenization process, which is necessary to attain the final stoichiometry from the initial bromide-rich phase. The homogenization process is associated with a reconstruction of the PbX_6 polyhedrons, with iodide diffusing toward the nuclei interior while bromide diffusing outward, or even halide migration across the interfaces. Unlike cation exchange or "molecular" exchange processes reported to assist the growth of high-quality thin-film perovskites (22, 23), homogenization and self-diffusion of the anions during the nucleation and growth stages have rarely been studied for thin-film perovskites. Such processes have been shown to assist defect formation in other material systems, especially when interstitial diffusion and vacancy-assisted diffusion are the dominant pathways to homogenize the halides (24, 25). We thus speculated that during the growth stage of $FAMACsPb(I_{0.8}Br_{0.2})_3$, these exchange and diffusion processes during homogenization promoted the formation of intrinsic defects associated with the halides, including vacancies, interstitials, and antisites. Our previous reports have shown the detrimental effects of point defects in perovskite materials, including V_I, Pb_I, and I_i (9, 26, 27). Complementarily, the strong PbI_2 peak intensity observed by XRD for the fully annealed $FAMACsPb(I_{0.8}Br_{0.2})_3$ films suggests that the organic A-site cations were less stable and decompose more readily with higher Br% incorporation, which is supported by further theoretical calculations that show V_{FA} and FA_i were thermodynamically more favored to form when the Br% increases from 0 to 20% (fig. S18).

To investigate the defect density and nature of the films, we first compared the optoelectronic properties of the films using time-resolved PL (TRPL) measurements shown in Fig. 3C. A much shorter carrier lifetime of $\tau = 382.8$ ns is observed for the $FAMACsPb(I_{0.8}Br_{0.2})_3$ film compared to the $\tau = 842.6$ ns of $FAMACsPbI_3$. In addition, we measured the quantified PL of the films and extracted the quasi-Fermi level splitting (qFLs) (Fig. 3D) based on a method we previously reported (28). The results show that the increasing qFLs did not track the bandgap increase with higher Br% incorporation. Twenty percent of Br incorporation resulted in the largest V_{OC} losses ($V_{OC,SQ}$ − qFLs at 1 sun; Fig. 3E), and the voltage loss was reduced as Br% decreased. The large V_{OC} loss for the 0% Br sample is potentially due to α-phase degradation by exposure to high ambient humidity of ~40% relative humidity during sample measurement. Halide segregation during illumination was negligible for the $FAMACsPb(I_{0.8}Br_{0.2})_3$ film due to its highly optimized composition, as seen by its stable emission peak positions retained during continuous PL measurements (Fig. 3F).

Positron annihilation spectroscopy (PAS) uses positively charged positrons that annihilate with negatively charged/neutral defects, capable of nondestructively probing the density and spatial distribution of defects in semiconductor thin films, and has been reported to be compatible with halide perovskite materials (29, 30). Compared

with admittance spectroscopy that also provides information about trap density, PAS could be carried out directly on bare perovskite films and is therefore independent of experimental variables that affect admittance spectroscopy results, such as the bandgap of the materials (which affects the device built-in potential) and the properties of the contacting transport materials (31). By controlling the kinetic energy of the incident positron beam and extracting the shape parameter from the gamma ray annihilation spectra (where a stronger gamma ray signal from positron annihilation could derive a larger shape parameter, indicating a higher density of negatively charged/neutral defects), a depth-resolved spectrum was obtained in Fig. 3G for the $FAMACsPb(I_{0.8}Br_{0.2})_3$ and $FAMACsPbI_3$ films. We observed that the shape parameter for $FAMACsPb(I_{0.8}Br_{0.2})_3$ was clearly higher throughout the entire perovskite film, indicating a higher overall trap density. The surface region (shaded in green, 0 to 50 nm, Fig. 3G) contained a much higher density of surface defects, which will be detrimental to both the device performance and stability. $FAMACsPb(I_{0.8}Br_{0.2})_3$ also had a higher shape parameter in the perovskite bulk region (shaded in orange, 150 to 500 nm, Fig. 3G), indicating a higher trap density throughout the entire film. Crucially, this indicates that the defects formed through intrinsic processes (i.e., during perovskite formation and growth). In contrast, extrinsic processes (e.g., degradation) would have initiated from the film surface, preserving the bulk trap density of the film (32, 33). Statistical analysis of the shape parameters comparing the surface and bulk regions is displayed in Fig. 3H. The eventual performance of the solar cell devices is a reflective consequence of the distinct defect physics and carrier dynamics of the films. As shown in Fig. 4A, devices based on both compositions exhibited >79% fill factor (FF), while the J_{SC} of $FAMACsPb(I_{0.8}Br_{0.2})_3$ (23.1 mA/cm^2) was distinctly lower than that of $FAMACsPbI_3$ (25.1 mA/cm^2) due to the larger bandgap of the former. The external quantum efficiency (EQE) cutoffs (Fig. 4B) of the devices also matched well with the bandgaps estimated by the ultraviolet-visible absorption and PL measurements. The V_{OC} gain of $FAMACsPb(I_{0.8}Br_{0.2})_3$ over $FAMACsPbI_3$, however, was insufficient to compensate for the bandgap increase, with V_{OC} values of 1.16 and 1.19 V ($V_{OC,SQ}$ − V_{OC} of 0.13 and 0.20 V, qE_g − V_{OC} of 0.40 and 0.48 V), respectively. The solar cell performance results coincided with the film characterization results, where nonradiative recombination losses were more severe for the $FAMACsPb(I_{0.8}Br_{0.2})_3$ perovskite. A stability test was also carried out, from which the $FAMACsPbI_3$ devices exhibited a much better long-term stability under illumination than $FAMACsPb(I_{0.8}Br_{0.2})_3$ devices after encapsulation (fig. S20). However, we found that the nonencapsulated devices of $FAMACsPbI_3$ decayed at a much faster rate, which is consistent with our observation during the PL quantum yield (PLQY) tests regarding the fatal extrinsic instability (most likely due to moisture-induced phase transformation) of the $FAMACsPbI_3$ perovskite. Detailed discussion on stability test is available in Supplementary Text.

DISCUSSION
On the basis of all our experimental and theoretical observations and results, we summarize the physical model of the formation dynamics of WBG mixed-halide perovskites in Fig. 4C. The inclusion of bromide in the composition altered the perovskite crystallization pathway. A bromide-rich phase was more thermodynamically stable and thus nucleates first from solution during supersaturation. To attain the final target stoichiometry, during the growth stage, a halide
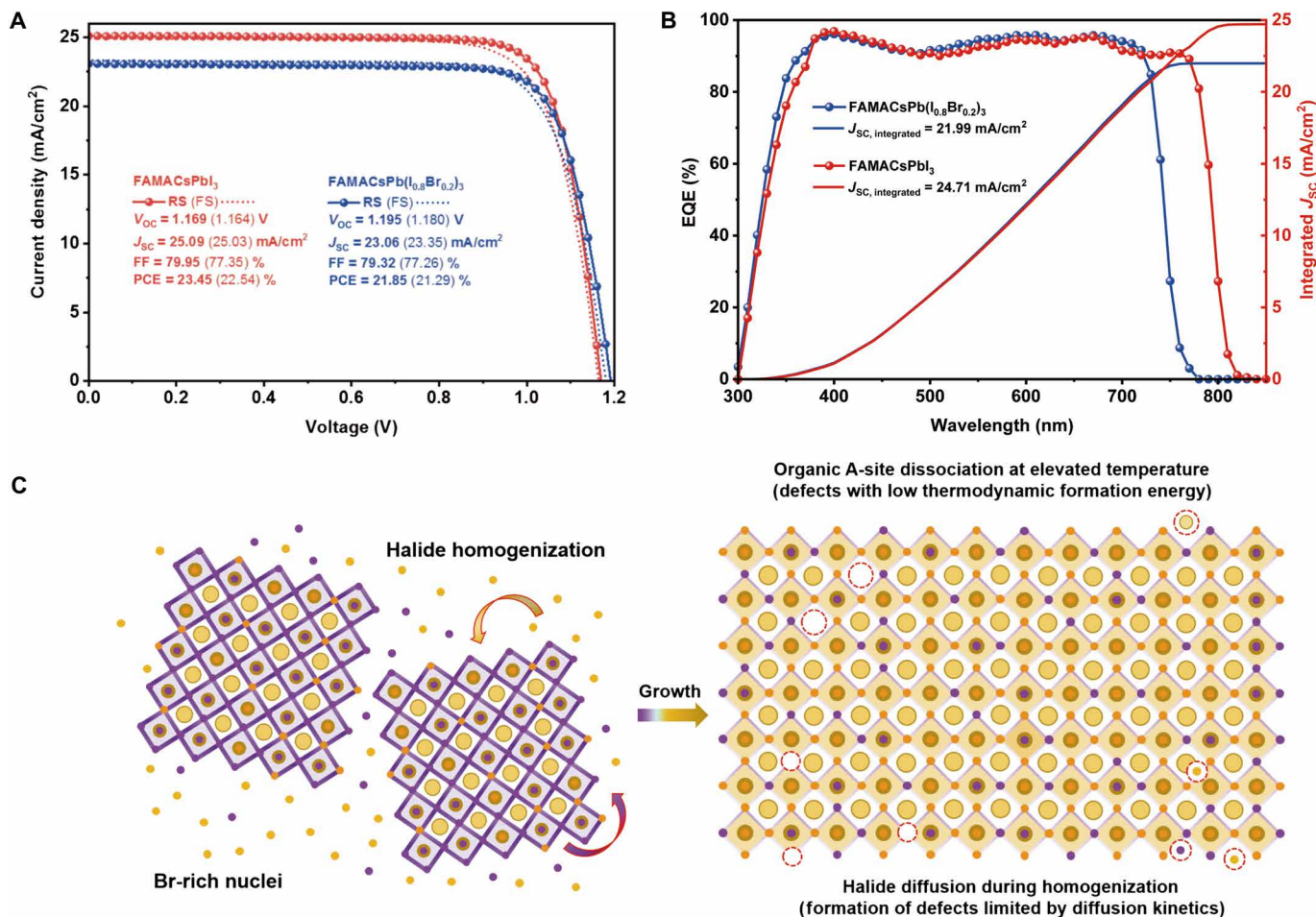
Fig. 4. Solar cell devices and the proposed physical model. *J-V* characteristics (**A**) and EQE spectrum (**B**) of perovskite solar cell devices based on CsFAMAPb(I$_{0.8}$Br$_{0.2}$)$_3$ and CsFAMAPbI$_3$. (**C**) A hypothetic physical model of formation kinetics in mixed-halide perovskite with high Br% (left) and their potential role with defect physics (right). Violet dots stand for bromine, and yellow dots stand for iodine. Several but not all possible point defects were illustrated at the surface or in the bulk. For simplification purpose, only the halides were specified for Br as purple dots and I as yellow dots.

homogenization process by diffusion gradually incorporates iodine into the expanding perovskite lattice. However, intrinsic defects formed readily during the homogenization process, and consequently, the final film had a higher defect density across the entire film depth, compared to the corresponding triiodide composition. Consequently, the WBG composition suffered from more severe nonradiative recombination losses and thus inferior optoelectronic properties and device performance. In this work, we correlated the complex perovskite formation dynamics with the defect physics and charge carrier dynamics of the resulting film. This study will guide the community to rethink the significance of precursor engineering and crystallization control for WBG mixed-halide perovskites toward more efficient and stable PVs based on these materials.

MATERIALS AND METHODS
Materials
DMF (99.8%), DMSO (99.7%), isopropanol (IPA; 99.7%), chlorobenzene (CB; 99.8%), acetonitrile (ACN; 99.8%), 4-tert-butyl pyridine (98%), lithium bis(trifluoromethanesulfonyl)imide (Li-TFSI; 99.95%), tris(2-(1*H*-pyrazol-1-yl)-4-*tert*-butylpyridine)cobalt(III)

tri[bis(trifluoromethane)sulfonimide] [FK 209 Co(III) TFSI salt], and PbI$_2$ (99.999%, perovskite grade) were purchased from Sigma-Aldrich. PbBr$_2$ (99.999%), CsI (99.998%), deionized water, and SnO$_2$ colloidal solution (15% in water) were purchased from Alfa Aesar. Formamidine iodide (FAI), formamidine bromide (FABr), methylammonium iodide (MAI), methylammonium bromide (MABr), and *n*-octylammonium iodide (OAI) were purchased from GreatCell Solar Materials (Australia). Methylammonium chloride (MACl) and Spiro-OMeTAD (99.8%) were purchased from Xi'an Polymer Light Technology (China). All the materials were used without further purification.

Perovskite precursor preparation
FAMACs-based perovskites
CsI (35.8 mg/ml), FAI (192.6 mg/ml), MAI (22.3 mg/ml), and PbI$_2$ (645.4 mg/ml) were dissolved in a DMF/DMSO = 80:20 solvent for the FAMACsPbI$_3$ precursor. For FAMACsPb(I$_{0.8}$Br$_{0.2}$)$_3$ precursor, CsI (35.8 mg/ml), FAI (168.6 mg/ml), PbI$_2$ (516.3 mg/ml), MABr (31.4 mg/ml), and PbBr$_2$ (102.8 mg/ml) were used. The final stoichiometries were (CsPbI$_3$)$_{0.1}$(FAPbI$_3$)$_{0.8}$(MAPbI$_3$)$_{0.1}$ and (CsPbI$_3$)$_{0.10}$(FAPbI$_3$)$_{0.7}$(MAPbBr$_3$)$_{0.2}$, respectively. Five to 50% Br

precursors were prepared by partially or fully substitute $MAPbI_3$ in the triiodide precursor by $MAPbBr_3$ correspondingly.

FACs-based perovskites

CsI (71.7 mg/ml), FAI (192.6 mg/ml), and PbI_2 (645.4 mg/ml) were dissolved in a DMF/DMSO = 80:20 solvent for the $FACsPbI_3$ precursor. For $FACsPb(I_{0.83}Br_{0.17})_3$ precursor, CsI (71.7 mg/ml), FAI (192.6 mg/ml), PbI_2 (480.8 mg/ml), and $PbBr_2$ (115.6 mg/ml) were used. The final stoichiometries were $FA_{0.8}Cs_{0.2}PbI_3$ and $FA_{0.8}Cs_{0.2}Pb(I_{0.83}Br_{0.17})_3$, respectively. Thirty mole percent of MACl were added in all perovskite precursors if without further specification. Ten to 50% Br precursors were prepared by maintaining the same cation ratio and only changing Br%.

Perovskite film preparation and solar cell fabrication

All processes were done in a N_2-filled glove box if without further specification. For the one-step FACs-perovskites and FAMACs-perovskites, the precursor solutions were casted to the substrate [either glass for in situ PL or glass/indium tin oxide (ITO)/SnO_2 for solar cells] and spin-coated at 3500 rpm. CB was casted to the films at 45 s, and we led the spin continued for another 60 s. After spin coating, the samples would be immediately transferred to a 65°C hot plate for a 5-min preannealing and then transferred to a 150°C hot plate in ambient for 10 min of full annealing. No extra passivation treatment was carried out for the perovskite film characterizations.

For solar cell fabrication, SnO_2 layer was prepared by spin coating a diluted SnO_2 colloidal solution on precleaned glass/ITO substrates at 3000 rpm for 30 s followed with 30 min ambient annealing at 150°C. The perovskite layers were prepared on top of the SnO_2 layer. For the best device performance, the passivation layer was done by spin-coating OAI (10 mM in IPA) at 5000 rpm followed with 1 min of annealing at 100°C. Twenty-five microliters of Spiro-OMeTAD solution prepared by mixing 85.8 mg of spiro-MeOTAD, 33.8 μl of 4-tert-butylpyridine, 19.3 μl of Li-TFSI (520 mg ml^{-1} in ACN) solution, and 17.9 μl of FK 209 Co(III) TFSI salt (375 mg ml^{-1} in ACN) in 1 ml of CB was spin-coated at 3000 rpm on the perovskite surface. After aging in dry air overnight, 120-nm gold was then evaporated to form the metal electrodes.

Thin films and device characterizations

For in situ PL measurement, a homebuilt platform consists of a 532-nm laser diode and an Ocean Optics Spectrometer (Flame) coupled with optical fibers, optical filters, and several planoconvex lenses described in our previous reports were used (34, 35). The power density of the laser was approximately 100 mW/cm^2 as the intensity reaching the sample could vary as adjusting the setup. Integration time of each spectra was 100 ms during the measurement. Calibrated measurements for qFLs were carried out in another homebuilt PL setup also with 532-nm excitation. The laser beam is quantified by a charge-coupled device camera and a power meter to calculate the equivalent number of suns from the photon flux. The wavelength dependence of the spectrometer and the collection optics is corrected using a commercial calibration lamp with known spectrum. For the TRPL measurement, a PicoHarp 300 with time-correlated single-photon counting capabilities excited by the 640-nm pulse laser diode (PLD 800B, PicoQuant) with a repetition frequency of 200 kHz. A biexponential decay fitting model was used to extract the charge carrier lifetime. For the XRD measurement, an x-ray diffractometer (PANalytical) with Cu Kα radiation at a scan rate of 3° min^{-1} was used, and the contact angle was obtained by VCA optima 100. All

XRD measurements were carried out in ambient environment after transferring the samples out from the N_2-filled glove box. Scanning electron microscopy was captured by a Nova Nano 230 system. PAS measurement was carried out at the Washington State University positron beam. Experimental details and spectra analysis methods have been fully discussed in our previous publication (27). An empirical formula of $d = \frac{40\, E_k^{1.6}}{\rho}\left(\frac{nm \cdot g}{cm^3 keV^{1.6}}\right)$ was used to convert the kinetic energy of incident positron (E_k) into depth profile. The fraction of the annihilated gamma ray signal in a narrow central region that increase in relative intensity at positron trap sites was determined as the shape parameter. The J-V characteristics were measured with a Keithley 2401 meter under the illumination of an Oriel Sol3A class AAA solar simulator (Newport) that simulated AM 1.5 G spectrum (100 mW/cm^2) calibrated with an NREL-certified Si photodiode with KG-5 filter. The EQE was measured by an Enlitech designed system under AC mode without bias light.

DFT calculations

All quantum chemical calculations of interaction energies between DMSO and PbXX′ were performed using Gaussian 16.1 (36). The initial structures used in computations were constructed using GaussView 6.0.16. PbXX′ was positioned at various locations around the DMSO, and the geometry of each resulting DMSO:PbXX′ complex was optimized with the ωB97X-D density functional and the 6-31+G(d,p) basis set for C, H, O, S, and Br atoms and LANL2DZ basis set for Pb and I atoms. Optimized geometries were verified as minima (zero imaginary frequencies) by frequency calculations at the same level of theory. Interaction energies were computed using the same level of theory and using the following equation: $\Delta E_{int} = E_{(DMSO:PbXX')} - [E_{DMSO} + E_{PbXX'}]$. Molecular structures were visualized and rendered using Mercury 4.3.1 (Build 273956). (37–39)

All first-principle calculations for bulk and slab systems are carried out using the Vienna Ab initio Simulation Package (VASP) code.(40, 41). A revised Perdew-Burke-Ernzerhof generalized gradient approximation (PBEsol) (42, 43) was used for the exchange correlation including a dispersion correction using Grimme's DFT-D3 scheme (44, 45). PBEsol functional has been introduced to improve the equilibrium properties of solids and surfaces (46). Valence-core interactions were described by projector augmented wave pseudopotentials (47). Plane wave expansions with kinetic energies up to 300 eV were chosen as the basis set for all geometry optimization and energy calculations. Both atomic positions and cell dimensions were optimized using a conjugate gradient algorithm until all Hellman-Feynman forces are smaller than 0.02 eV/Å. Γ-center k-point mesh ($4 \times 4 \times 4$ and $4 \times 4 \times 1$) was adopted for Brillouin zone sampling in bulk and surface calculations, respectively.

For formation energies of DMSO:PbXX′ adduct crystals, we used the following expression: $\Delta H(DMSO : PbXX') = H(DMSO : PbXX') - [H(DMSO) + H(PbXX')]$, where the first, second, and third terms in the right hand side are the energies of DMSO:PbXX′, DMSO, and PbXX′, respectively. We considered XX′ = I_2, IBr, and Br_2 and used the monoclinic DMSO in all cases, and the crystal structures of DMSO:PbXX′ and PbXX′ are based on orthorhombic DMSO:PbI_2 and hexagonal PbI_2 crystals, respectively.

For surface energy calculations, the $2 \times 2 \times L$ surfaces were formed along (001) by periodic slabs including 9 to 11 atomic layers for a surface separated by 10 to 15 Å of vacuum. To characterize the formation and stability of the ABX_3 surfaces, we use surface energies

described as follows: we first calculate the cleavage energy of the clean surface

$$\sigma^{clv} = \frac{1}{2}\Big[E_{slab}^{unrel} - NE_{bulk} + \sum_i n_i\mu_i\Big] \quad (1)$$

where the first term is the energy of the unrelaxed slab, μ_i is the chemical potentials, n_i is the number of ith unit removed, and $E_{bulk} = \mu_A + \mu_{Pb} + 3\mu_X$ is the energy per formula unit of the bulk perovskite. The relaxation energy is then calculated from

$$\sigma^{rl} = E_{slab}^{rel} - E_{slab}^{unrel} \quad (2)$$

where the first and second terms are the total energy of the relaxed and unrelaxed slabs, respectively. The surface energy is calculated by $\gamma = (\sigma^{clv} + \sigma^{rel})/A$, where A is the area of the surface. For the $APbX_3$ perovskite, A = FA, MA, or Cs and X = Br or I were calculated independently. For this study, we considered PbX_2-terminated surfaces.

Formation energies of the defects in $FAPb(I_xBr_{1-x})_3$ in a charge-state q is calculated from

$$\Delta H_d(q) = E_d(q) - E_{pr} + \sum_i n_i\mu_i' + q(E_F + E_{VBM}) \quad (3)$$

where $E_d(q)$ is the total energy of the system with defect and E_{pr} is the pristine system. $\mu_i' = \mu_{0i} + \mu_i$ is the chemical potential, which includes intrinsic μ_{0i} and growth condition–dependent term μ_i. n_i is the number of ith unit (i.e., atom or molecule) exchanged with the reservoir to form the defect. E_F is the Fermi energy, and E_{VBM} is the energy at the valence band maximum. Following Freysoldt's correction scheme, the energy corrections arising from the spurious interactions due to the finite-size are included in Eq. 3.

To determine the chemical potentials required for formation energy of a $FAPb(I_xBr_{1-x})_3$

$$\mu_{FA} + \mu_{Pb} + 3\big[x\mu_I + (1-x)\mu_{Br}\big] = \Delta H_1 \quad (4)$$

should be satisfied under thermodynamic equilibrium growth conditions, where ΔH_1 is the formation energy of $FAPb(I_xBr_{1-x})_3$. In this study, we considered x = 1, 0.8, and 0. To avoid the formation of undesired phases

$$\mu_{FA} + \mu_I < \Delta H(FAI), \mu_{FA} + \mu_{Br} < \Delta H(FABr) \quad (5)$$

$$\mu_{Pb} + 2\mu_I < \Delta H(PbI_2), \mu_{Pb} + 2\mu_{Br} < \Delta H(PbBr_2) \quad (6)$$

conditions should also be satisfied where appropriate. The formation energies in the right hand sides of Eqs. 5 and 6 are calculated from $\Delta H(FABr) = H(FABr) - \big[H(FA) + \frac{1}{2}H(Br_2)\big]$, $\Delta H(FAI) = H(FAI) - \big[H(FA) + \frac{1}{2}H(I_2)\big]$, $\Delta H(PbI_2) = H(PbI_2) - [H(Pb) + H(I_2)]$, and $\Delta H(PbBr_2) = H(PbBr) - [H(Pb) + H(Br_2)]$. Here, to calculate each energy term, we used the respective structures: FABr and FAI in the rock-salt phases, PbI_2 and $PbBr_2$ in the hexagonal phases, FA in the body-centered cubic phase, Pb in the cubic phase, and I_2 and Br_2 in the gas phase. We considered the Pb-rich growth conditions in all chemical potential calculations.

SUPPLEMENTARY MATERIALS

REFERENCES AND NOTES

1. M. Green, E. Dunlop, J. Hohl-Ebinger, M. Yoshita, N. Kopidakis, X. Hao, Solar cell efficiency tables (version 57). *Prog. Photovolt. Res. Appl.* **29**, 3–15 (2021).
2. D. P. Mcmeekin, G. Sadoughi, W. Rehman, G. E. Eperon, M. Saliba, M. T. Hörantner, A. Haghighirad, N. Sakai, L. Korte, B. Rech, M. B. Johnston, L. M. Herz, H. J. Snaith, A mixed-cation lead mixed-halide perovskite absorber for tandem solar cells. *Science* **351**, 151–155 (2016).
3. Best Research-Cell Efficiency Chart (2021); www.nrel.gov/pv/cell-efficiency.html.
4. M. Jeong, I. W. Choi, E. M. Go, Y. Cho, M. Kim, B. Lee, S. Jeong, Y. Jo, H. W. Choi, J. Lee, J.-H. Bae, S. K. Kwak, D. S. Kim, C. Yang, Stable perovskite solar cells with efficiency exceeding 24.8% and 0.3-V voltage loss. *Science* **369**, 1615–1620 (2020).
5. A. Al-Ashouri, E. Köhnen, B. Li, A. Magomedov, H. Hempel, P. Caprioglio, J. A. Márquez, A. B. Morales Vilches, E. Kasparavicius, J. A. Smith, N. Phung, D. Menzel, M. Grischek, L. Kegelmann, D. Skroblin, C. Gollwitzer, T. Malinauskas, M. Jošt, G. Matič, B. Rech, R. Schlatmann, M. Topič, L. Korte, A. Abate, B. Stannowski, D. Neher, M. Stolterfoht, T. Unold, V. Getautis, S. Albrecht, Monolithic perovskite/silicon tandem solar cell with >29% efficiency by enhanced hole extraction. *Science* **370**, 1300–1309 (2020).
6. G.-W. Kim, A. Petrozza, Defect tolerance and intolerance in metal-halide perovskites. *Adv. Energy Mater.* **10**, 2001959 (2020).
7. K. X. Steirer, P. Schulz, G. Teeter, V. Stevanovic, M. Yang, K. Zhu, J. J. Berry, Defect tolerance in methylammonium lead triiodide perovskite. *ACS Energy Lett.* **1**, 360–366 (2016).
8. Z. Ni, C. Bao, Y. Liu, Q. Jiang, W.-Q. Wu, S. Chen, X. Dai, B. Chen, B. Hartweg, Z. Yu, Z. Holman, J. Huang, Resolving spatial and energetic distributions of trap states in metal halide perovskite solar cells. *Science* **367**, 1352–1358 (2020).
9. R. Wang, J. Xue, K.-L. Wang, Z.-K. Wang, Y. Luo, D. Fenning, G. Xu, S. Nuryyeva, T. Huang, Y. Zhao, J. L. Yang, J. Zhu, M. Wang, S. Tan, I. Yavuz, K. N. Houk, Y. Yang, Constructive molecular configurations for surface-defect passivation of perovskite photovoltaics. *Science* **366**, 1509–1513 (2019).
10. M. Qin, T.-K. Tse, T.-K. Lau, Y. Li, C.-J. Su, G. Yang, J. Chen, J. Zhu, U.-S. Jeng, G. Li, H. Chen, X. Lu, Manipulating the mixed-perovskite crystallization pathway unveiled by in situ GIWAXS. *Adv. Mater.* **31**, 1901284 (2019).
11. J.-P. Correa-Baena, Y. Luo, T. M. Brenner, J. Snaider, S. Sun, X. Li, M. A. Jensen, N. T. P. Hartono, L. Nienhaus, S. Wieghold, J. R. Poindexter, S. Wang, Y. S. Meng, T. Wang, B. Lai, M. V. Holt, Z. Cai, M. G. Bawendi, L. Huang, T. Buonassisi, D. P. Fenning, Homogenized halides and alkali cation segregation in alloyed organic-inorganic perovskites. *Science* **363**, 627–631 (2019).
12. R. E. Beal, N. Z. Hagström, J. Barrier, A. Gold-Parker, R. Prasanna, K. A. Bush, D. Passarello, L. T. Schelhas, K. Brüning, C. J. Tassone, H.-G. Steinrück, M. D. McGehee, M. F. Toney, A. F. Nogueira, Structural origins of light-induced phase segregation in organic-inorganic halide perovskite photovoltaic materials. *Matter* **2**, 207–219 (2020).
13. S. Mahesh, J. M. Ball, R. D. J. Oliver, D. P. McMeekin, P. K. Nayak, M. B. Johnston, H. J. Snaith, Revealing the origin of voltage loss in mixed-halide perovskite solar cells. *Energ. Environ. Sci.* **13**, 258–267 (2020).
14. C. M. Sutter-Fella, Q. P. Ngo, N. Cefarin, K. L. Gardner, N. Tamura, C. V. Stan, W. S. Drisdell, A. Javey, F. M. Toma, I. D. Sharp, Cation-dependent light-induced halide demixing in hybrid organic–inorganic perovskites. *Nano Lett.* **18**, 3473–3480 (2018).
15. E. S. Parrott, J. B. Patel, A.-A. Haghighirad, H. J. Snaith, M. B. Johnston, L. M. Herz, Growth modes and quantum confinement in ultrathin vapour-deposited MAPbI3 films. *Nanoscale* **11**, 14276–14284 (2019).
16. T.-B. Song, Z. Yuan, F. Babbe, D. P. Nenon, E. Aydin, S. De Wolf, C. M. Sutter-Fella, Dynamics of antisolvent processed hybrid metal halide perovskites studied by in situ photoluminescence and its influence on optoelectronic properties. *ACS Appl. Energy Mater.* **3**, 2386–2393 (2020).
17. T.-B. Song, Z. Yuan, M. Mori, F. Motiwala, G. Segev, E. Masquelier, C. V. Stan, J. L. Slack, N. Tamura, C. M. Sutter-Fella, Revealing the dynamics of hybrid metal halide perovskite formation via multimodal in situ probes. *Adv. Funct. Mater.* **30**, 1908337 (2020).
18. L. Gao, G. Yang, Organic-inorganic halide perovskites: From crystallization of polycrystalline films to solar cell applications. *Sol. RRL* **4**, 1900200 (2020).
19. J.-W. Lee, S. Tan, T.-H. Han, R. Wang, L. Zhang, C. Park, M. Yoon, C. Choi, M. Xu, M. E. Liao, S.-J. Lee, S. Nuryyeva, C. Zhu, K. Huynh, M. S. Goorsky, Y. Huang, X. Pan, Y. Yang, Solid-phase hetero epitaxial growth of α-phase formamidinium perovskite. *Nat. Commun.* **11**, 5514 (2020).
20. J.-W. Lee, Z. Dai, C. Lee, H. M. Lee, T.-H. Han, N. De Marco, O. Lin, C. S. Choi, B. Dunn, J. Koh, D. Di Carlo, J. H. Ko, H. D. Maynard, Y. Yang, Tuning molecular interactions for highly reproducible and efficient formamidinium perovskite solar cells via adduct approach. *J. Am. Chem. Soc.* **140**, 6317–6324 (2018).
21. N. Ahn, D.-Y. Son, I.-H. Jang, S. M. Kang, M. Choi, N.-G. Park, Highly reproducible perovskite solar cells with average efficiency of 18.3% and best efficiency of 19.7% fabricated via Lewis base adduct of lead(II) iodide. *J. Am. Chem. Soc.* **137**, 8696–8699 (2015).

22. Y.-M. Xie, B. Yu, C. Ma, X. Xu, Y. Cheng, S. Yuan, Z.-K. Wang, H. T. Chandran, C.-S. Lee, L.-S. Liao, S.-W. Tsang, Direct observation of cation-exchange in liquid-to-solid phase transformation in $FA_{1−x}MA_xPbI_3$ based perovskite solar cells. *J. Mater. Chem. A* **6**, 9081–9088 (2018).

23. W. S. Yang, J. H. Noh, N. J. Jeon, Y. C. Kim, S. Ryu, J. Seo, S. I. Seok, High-performance photovoltaic perovskite layers fabricated through intramolecular exchange. *Science* **348**, 1234–1237 (2015).

24. S. Exarhos, E. Palmes, L. Mangolini, Structural homogenization and cation ordering in CZTS films during sulfurization as probed via in-situ Raman. *Thin Solid Films* **684**, 21–30 (2019).

25. H. P. Ho, I. Harrison, N. Baba-Ali, B. Tuck, Diffusion-induced defects in GaAs by zinc and the effects of post-diffusion anneal. *J. Appl. Phys.* **69**, 3494–3502 (1991).

26. Y. Zhao, P. Zhu, S. Huang, S. Tan, M. Wang, R. Wang, J. Xue, T.-H. Han, S.-J. Lee, A. Zhang, T. Huang, P. Cheng, D. Meng, J.-W. Lee, J. Marian, J. Zhu, Y. Yang, Molecular interaction regulates the performance and longevity of defect passivation for metal halide perovskite solar cells. *J. Am. Chem. Soc.* **142**, 20071–20079 (2020).

27. S. Tan, I. Yavuz, M. H. Weber, T. Huang, C.-H. Chen, R. Wang, H.-C. Wang, J. H. Ko, S. Nuryyeva, J. Xue, Y. Zhao, K.-H. Wei, J.-W. Lee, Y. Yang, Shallow iodine defects accelerate the degradation of α-phase formamidinium perovskite. *Joule* **4**, 2426–2442 (2020).

28. F. Babbe, L. Choubrac, S. Siebentritt, Quasi Fermi level splitting of Cu-rich and Cu-poor $Cu(In,Ga)Se_2$ absorber layers. *Appl. Phys. Lett.* **109**, 082105 (2016).

29. S. Tan, T. Huang, I. Yavuz, R. Wang, M. H. Weber, Y. Zhao, M. Abdelsamie, M. E. Liao, H.-C. Wang, K. Huynh, K.-H. Wei, J. Xue, F. Babbe, M. S. Goorsky, J.-W. Lee, C. M. Sutter-Fella, Y. Yang, Surface reconstruction of halide perovskites during post-treatment. *J. Am. Chem. Soc.* **143**, 6781–6786 (2021).

30. M.-F. Barthe, H. Labrim, A. Gentils, P. Desgardin, C. Corbel, S. Esnouf, J. P. Piron, Positron annihilation characteristics in UO2: For lattice and vacancy defects induced by electron irradiation. *Phys. Stat. Solidi C* **4**, 3627–3632 (2007).

31. S. S. Hegedus, W. N. Shafarman, Thin-film solar cells: Device measurements and analysis. *Prog. Photovolt. Res. Appl.* **12**, 155–176 (2004).

32. B. Chen, P. N. Rudd, S. Yang, Y. Yuan, J. Huang, Imperfections and their passivation in halide perovskite solar cells. *Chem. Soc. Rev.* **48**, 3842–3867 (2019).

33. D. Meggiolaro, E. Mosconi, F. De Angelis, Formation of surface defects dominates ion migration in lead-halide perovskites. *ACS Energy Lett.* **4**, 779–785 (2019).

34. M. Abdelsamie, J. Xu, K. Bruening, C. J. Tassone, H.-G. Steinrück, M. F. Toney, Impact of processing on structural and compositional evolution in mixed metal halide perovskites during film formation. *Adv. Funct. Mater.* **30**, 2001752 (2020).

35. M. Abdelsamie, T. Li, F. Babbe, J. Xu, Q. Han, V. Blum, C. M. Sutter-Fella, D. B. Mitzi, M. F. Toney, Mechanism of additive-assisted room-temperature processing of metal halide perovskite thin films. *ACS Appl. Mater. Interfaces* **13**, 13212–13225 (2021).

36. D. J. Frisch, M. J. Trucks, G. W. Schlegel, H. B. Scuseria, G. E. Robb, M. A. Cheeseman, J. R. Scalmani, G. Barone, V. Petersson, G. A. Nakatsuji, H. Li, X. Caricato, M. Marenich, A. V. Bloino, J. Janesko, B. G. Gomperts, R. Mennucci, B. Hratch, Gaussian 16, Revision A.03. *Gaussian Inc., Wallingford CT* (2016).

37. C. F. Macrae, I. Sovago, S. J. Cottrell, P. T. A. Galek, P. McCabe, E. Pidcock, M. Platings, G. P. Shields, J. S. Stevens, M. Towler, P. A. Wood, Mercury 4.0: From visualization to analysis, design and prediction. *J. Appl. Cryst.* **53**, 226–235 (2020).

38. C. F. Macrae, P. R. Edgington, P. McCabe, E. Pidcock, G. P. Shields, R. Taylor, M. Towler, J. van de Streek, Mercury: Visualization and analysis of crystal structures. *J. Appl. Cryst.* **39**, 453–457 (2006).

39. I. J. Bruno, J. C. Cole, P. R. Edgington, M. Kessler, C. F. Macrae, P. McCabe, J. Pearson, R. Taylor, New software for searching the Cambridge Structural Database and visualizing crystal structures. *Acta Crystallogr. B.* **58**, 389–397 (2002).

40. G. Kresse, J. Furthmüller, Efficiency of ab-initio total energy calculations for metals and semiconductors using a plane-wave basis set. *Comput. Mater. Sci.* **6**, 15–50 (1996).

41. G. Kresse, J. Furthmüller, Efficient iterative schemes forab initiototal-energy calculations using a plane-wave basis set. *Phys. Rev. B* **54**, 11169–11186 (1996).

42. J. P. Perdew, A. Ruzsinszky, G. I. Csonka, O. A. Vydrov, G. E. Scuseria, L. A. Constantin, X. Zhou, K. Burke, Restoring the density-gradient expansion for exchange in solids and surfaces. *Phys. Rev. Lett.* **100**, 136406 (2008).

43. J. P. Perdew, K. Burke, M. Ernzerhof, Generalized gradient approximation made simple. *Phys. Rev. Lett.* **77**, 3865–3868 (1996).

44. S. Grimme, J. Antony, S. Ehrlich, H. Krieg, A consistent and accurate ab initio parametrization of density functional dispersion correction (DFT-D) for the 94 elements H-Pu. *J. Chem. Phys.* **132**, 154104 (2010).

45. S. Grimme, Semiempirical GGA-type density functional constructed with a long-range dispersion correction. *J. Comput. Chem.* **27**, 1787–1799 (2006).

46. P. E. Blöchl, Projector augmented-wave method. *Phys. Rev. B* **50**, 17953–17979 (1994).

47. G. I. Csonka, J. P. Perdew, A. Ruzsinszky, P. H. T. Philipsen, S. Lebègue, J. Paier, O. A. Vydrov, J. G. Ángyán, Assessing the performance of recent density functionals for bulk solids. *Phys. Rev. B* **79**, 155107 (2009).